Numerical Simulations of Convectively Generated Stratospheric Gravity Waves

R. FOVELL,* D. DURRAN, AND J. R. HOLTON

Department of Atmospheric Sciences, University of Washington, Seattle, Washington

(Manuscript received 6 June 1991, in final form 6 November 1991)

ABSTRACT

The excitation and vertical propagation of gravity waves is simulated in a two-dimensional model of a mesoscale convective storm. It is shown that in a simulated squall line the gravity waves that are preferentially excited are those propagating opposite to the direction of motion of the storm. Solutions for cases with differing stratospheric mean zonal flow profiles are compared. It turns out that, in the absence of storm-relative mean winds in the stratosphere, the primary mode of excitation of gravity waves is by mechanical forcing owing to oscillatory updrafts. The stratospheric response consists of waves whose periods match the primary periods of the forcing. Owing to the tendency of the oscillating updrafts to propagate toward the rear of the storm, gravity wave propagation is limited primarily to the rearward direction, and there is a net downward momentum transport. When storm-relative mean winds are included in the model the waves excited by the oscillating updrafts are weaker, but a new class of waves, similar to topographic waves, appears in the stratosphere directly above the main updraft region.

The cloud model results are compared with results from a dry model in which waves are excited by a specified compact momentum source designed to mimic the mechanical forcing caused by the regular development and rearward propagation of updraft cells. Results from this analog strongly support the notion that squall-line–generated gravity waves arise from mechanical forcing rather than thermal effects.

1. Introduction

The zonal mean climate of the stratosphere is strongly influenced by the troposphere through the vertical transfer of momentum via waves originating in the troposphere. This dynamical coupling of the troposphere and stratosphere also has some effect on the circulation of the troposphere since the mean motion across the tropopause is to a large extent determined by eddy drag forces in the stratosphere (Haynes et al. 1991). Thus, an improved understanding of the mechanisms of dynamical coupling between the troposphere and stratosphere is desirable for development of better global forecast models; it is also essential for development of accurate global climate and chemical tracer models for the stratosphere.

The role of vertically propagating planetary waves in controlling the temperature and wind distribution in the winter stratosphere is now quite well understood, except perhaps for the high-latitude Southern Hemisphere. (See Andrews et al. 1987 for discussion and references.) Following the seminal paper of Lindzen (1981) there has been a growing appreciation for the importance of the dynamical coupling provided by gravity waves generated in the troposphere and propagating into the middle atmosphere, where they may break and influence the mean flow through wave drag and diffusion. This gravity wave drag effect appears to exert a first-order control on the circulation of the mesosphere (Holton 1983). Its role in the stratosphere is more controversial, although Rind et al. (1988) found that parameterized drag by topographic gravity waves was required to obtain a realistic mean flow distribution in the stratosphere in their medium resolution general circulation model (GCM). This is consistent with Mahlman and Umscheid (1987), who argue that planetary-wave Eliassen–Palm (EP) flux divergences are inadequate alone to provide the wave drag force required to maintain the observed mean zonal wind distribution in the winter stratosphere, which is much weaker than the radiative equilibrium mean flow.

In addition, McFarlane (1987) and Palmer et al. (1986) have shown that the tendency for middle-range global forecast models to produce excessively strong westerly jet streams (the climate drift problem) can be overcome by including a parameterized gravity wave drag in the upper troposphere and lower stratosphere (see also Miller et al. 1989). Thus, it appears that gravity wave drag is important for the momentum budget in the upper troposphere as well as in the middle atmosphere.

Unlike planetary waves, gravity waves are not resolved by the synoptic observational network. Our

* Present affiliation: Department of Atmospheric Sciences, UCLA, Los Angeles, California.

Corresponding author address: Dr. James R. Holton, Department of Atmospheric Sciences, AK-40, University of Washington, Seattle, WA 98195.

knowledge of their morphology depends on limited aircraft and rocket investigations together with remote sounding by mesosphere–stratosphere–troposphere (MST) radars at a few locations (Gage and Balsley 1984). Thus, there is still considerable uncertainty concerning the sources and distribution of internal gravity waves. Stationary waves generated by flow over topography (lee waves) have, of course, been studied for many years, although most efforts have concentrated on their effects in the troposphere rather than their penetration into the stratosphere (e.g., Durran 1986). Observations of gravity waves in the middle atmosphere (see Fritts 1984 for review) indicate that a large fraction of the gravity wave momentum flux is due not to stationary waves but to high-frequency waves, which suggests that sources other than topography must be important. One class of sources are mass–momentum adjustment processes, of which geostrophic adjustment (Rossby 1938) is the most familiar example. A three-dimensional model of the generation of vertically propagating gravity waves by geostrophic adjustment was presented by Zhu and Holton (1987).

Because cumulus convection involves strong transient vertical motions in a conditionally stable environment, convective storms should also be important sources of gravity waves. A few aircraft measurements (Pfister et al. 1986) have documented gravity wave motions in the tropical lower stratosphere in conjunction with outbreaks of cumulonimbus convection. Wave generation by shallow nonprecipitating cumulus clouds formed in convectively active planetary boundary layers has been studied observationally by Kuettner et al. (1987) and theoretically by Clark et al. (1986). Observational evidence for gravity wave generation by thunderstorms has been presented by several authors (e.g., Lu et al. 1984). The generation of gravity waves by deep convection has not, however, received much theoretical attention.

Superficially, it might seem that gravity wave generation by a cumulus cloud could be assessed by modeling the convection as a transient heat source. This would simplify the problem since production of linear gravity waves by specified heat sources can be studied by standard analytic methods (Smith and Lin 1982; Bretherton 1988). This is, however, not an adequate approach for studying convectively generated gravity waves. Cumulus clouds are not simply time-dependent heat sources. The pressure and momentum fields associated with the clouds will strongly influence the generation of gravity waves, especially in the presence of environmental wind shears.

Clark et al. (1986) argued that there are two mechanisms through which the pressure and momentum fields associated with convective eddies can generate gravity waves in an overlying stable layer. In the first of these, which they called "thermal" forcing, oscillating updrafts and downdrafts impinging on the interface between the unstable and stable regions cause oscillating displacements of the isentropes at the base of the stable layer, which in turn excite vertically propagating gravity waves. This mechanism will be labeled here the "mechanical oscillator effect" since it is closely analogous to the mechanical oscillator forcing used in laboratory simulations of transient internal gravity waves by Mowbray and his collaborators (see Lighthill 1978 for an excellent summary and references to the original literature).

The second mechanism discussed by Clark et al. (1986) was referred to by them as the "obstacle effect." (This effect was earlier discussed by Mason and Sykes 1982.) Clark et al. indicated that this type of gravity wave forcing occurs when the pressure field produced by a *rising* convective element acts as an obstruction to the environmental horizontal flow, thus generating waves. A similar forcing can, of course, be generated by the pressure field associated with a convective *downdraft*. In either case the mechanism is most effective when there are persistent updrafts or downdrafts, as may occur in mesoscale convective systems. Thus, this mechanism will be called "quasi-stationary forcing" in order to avoid the implication that it arises only because clouds act like equivalent mountains.

These two effects can be distinguished since the mechanical oscillator effect does not require any mean flow relative to the convective element, while the quasi-stationary forcing effect does. Clark et al. (1986) found that in their two-dimensional numerical model strong waves were generated only in the presence of environmental wind shear. Thus, they concluded that the latter effect was the more important wave generator, at least for shallow boundary-layer convection.

It is by no means clear whether the obstacle effect would also dominate in gravity wave generation associated with the deep convection characteristic of an organized mesoscale convective storm. In this paper a high-resolution two-dimensional nonhydrostatic numerical model is used to simulate long-lived squall lines for various mean wind conditions and to examine the characteristics of the vertically propagating gravity waves associated with such systems. It turns out that significant gravity wave propagation into the stratosphere occurs in this model even when the mean flow relative to the storm in the upper troposphere and lower stratosphere is very weak. Thus, quasi-stationary forcing is not the only important wave-generating mechanism in these simulations. Rather, it appears that parcel oscillations associated with convective updraft and downdraft cells within the squall line act as nearly periodic mechanical oscillators, which excite gravity waves in the model through the mechanical oscillator effect.

Internal gravity waves are primarily of interest because they can transfer momentum vertically, and thus provide an important mechanism whereby the stratosphere can be forced remotely from the troposphere. Vertically propagating waves generated in the tropo-

sphere with westerly (easterly) phase speeds relative to the mean flow transfer westerly (easterly) momentum into the stratosphere. At levels where the waves are dissipated (e.g., by wave breaking) there will be a momentum flux divergence and mean flow forcing by the waves. The efficacy of such waves in providing net forcing of the mean flow depends crucially on the wave spectrum. For example, if waves of equal amplitude and opposite phase speeds are generated, the domain-averaged momentum flux at any level will vanish since the contributions from the westerly and easterly wave packets will identically cancel. On the other hand, if waves with either positive or negative phase speeds should dominate, either because they are selectively excited or selectively transmitted, then a net wave-driven zonal force will occur at any level where they are dissipated.

It is shown later that simulated two-dimensional squall lines preferentially excite gravity waves whose storm-relative phase propagation is opposite to the direction of motion of the storm. Solutions for cases with differing stratospheric mean zonal flow profiles are contrasted. The cloud model results are also compared with results from a dry model in which gravity waves are driven by a specified mechanical forcing in order to test the hypothesis that squall-line-generated gravity waves arise mainly from mechanical forcing owing to vertical displacements associated with oscillatory updrafts and downdrafts.

2. The numerical model

a. Governing equations

The convective storm simulations were made with the two-dimensional variant of the mesoscale model of Durran and Klemp (1983) used in Miller and Durran (1991). This is a compressible model that is dynamically and physically similar to that of Klemp and Wilhelmson (1978). In particular, it employs the simple microphysics of Klemp and Wilhelmson, which excludes ice processes. The horizontal and vertical momentum equations, the continuity equation written in terms of the pressure field, and the thermodynamic energy equation are given, respectively, by

$$\frac{\partial(\rho u)}{\partial t} + \frac{\partial(\rho u^2)}{\partial x} + \frac{\partial(\rho uw)}{\partial z} + \frac{\partial p}{\partial x} = \rho D_u \quad (1a)$$

$$\frac{\partial(\rho w)}{\partial t} + \frac{\partial(\rho uw)}{\partial x} + \frac{\partial(\rho w^2)}{\partial z} + \frac{\partial p}{\partial z} = -(\rho - \bar{\rho})g + \rho D_w \quad (1b)$$

$$\frac{\partial p}{\partial t} + \frac{c_p p}{c_v \rho}\left[\frac{\partial(\rho u)}{\partial x} + \frac{\partial(\rho w)}{\partial z}\right] = \frac{c_p p}{c_v \theta}\frac{\partial \theta}{\partial t} \quad (1c)$$

$$\frac{\partial \theta}{\partial t} + u\frac{\partial \theta}{\partial x} + w\frac{\partial \theta}{\partial z} = D_\theta. \quad (1d)$$

The terms D_u, D_w, and D_θ on the right in (1a), (1b), and (1d), respectively, denote subgrid-scale mixing. They are determined using the Richardson number–dependent first-order closure scheme given in Durran and Klemp (1983). The term $\bar{\rho}$ in (1b) denotes the horizontally averaged mean-state density field; all other symbols have their conventional meanings.

The system is completed by the equation of state, which relates the pressure field to the density and temperature fields, and continuity equations for water vapor, cloud water, and rainwater. These are given explicitly in Durran and Klemp (1983). The solution proceeds by a two-time-step process in which a small time step is used for stable integration of the high-speed sound wave modes, while the bulk of the computations is carried out with a larger time step. Details of this procedure can be found in Klemp and Wilhelmson (1978). The model is initialized with a horizontally homogeneous basic state.

Squall line models have generally sacrificed resolution in the stratosphere in order to better resolve the troposphere. In some models variable vertical grid resolution has been used, with higher resolution in the lower troposphere and lower resolution in the stratosphere. In addition, a rigid-lid upper boundary condition has often been employed, and the stratosphere has usually been treated as a region of large diffusion. Provided that the model domain extends through a couple of scale heights in the stratosphere, the rigid upper boundary and reduced resolution in the stratosphere may not affect the tropospheric portion of the storm very much, but these factors can severely affect the character of vertically propagating stratospheric gravity waves.

In order to simulate such waves faithfully, a careful treatment of the stratosphere is required. To avoid rapid dissipation of gravity waves, the background diffusion in the model is set to comparatively small values. Horizontal background diffusion is fourth order for greater scale selectivity; the nondimensional smoothing coefficient [γ in Eq. (35) of Durran and Klemp 1983] is 0.012. This same coefficient is used for the vertical background diffusion, which is also fourth or der, but is applied only to the vertical velocity and pressure fields, as was done by Miller and Durran (1991) in their mountain wave studies. The radiation upper boundary condition of Klemp and Durran (1983) is employed to prevent reflection of vertically propagating gravity waves.

The model domain is 720 km wide and 30 km deep, and is represented by a grid mesh of 480 by 134 points, respectively. High vertical resolution is used throughout the depth of the model atmosphere, with the highest resolution in the stratosphere. The vertical grid interval chosen near the surface, 400 m, is sufficient to resolve important storm features at low levels; resolution is gradually improved to 175 m near the top boundary, which should be sufficient to resolve possible wave

breaking in the stratosphere. The grid interval is constant in the horizontal direction at 1500 m; the short time step is 2 s and the long time step is 6 s. The lateral boundary conditions are the same as those used by Klemp and Wilhelmson (1978); the phase-speed parameter chosen to minimize wave reflection at the lateral boundaries was $c^* = 35$ m s^{-1}.

b. *Sensitivity tests*

The numerical simulations exhibited some sensitivity to both the upper and the lateral boundary conditions. When the radiation condition was imposed at the top of very deep domains (i.e., greater than 25 km deep) the model tended to develop a spurious shallow layer of cooling just beneath the upper boundary. Experiments in which the domain was progressively deepened demonstrated that the solution at a fixed level improved as domain depth was increased, but the cooling next to the upper boundary became more intense. In some cases, the cooling produced rapidly growing disturbances near the upstream boundary that terminated the simulation. This cooling tendency was controlled by adding a weak "sponge layer" to the top 5 km of the numerical domain. The damping rate in the sponge layer was sufficient only to counteract the tendency toward mean cooling near the upper boundary. It was too weak to significantly reduce the velocity perturbations in waves traversing it, and the radiation condition of Klemp and Durran (1983) was still required to prevent spurious wave reflection.

Lateral-boundary sensitivity tests, similar to those reported by Fovell and Ogura (1988), were also conducted. These tests included varying both the width of the computational domain and the magnitude of the gravity wave speed parameter (c^*) in the lateral boundary condition. Originally, the variable c^* boundary condition of Orlanski (1976) was employed, but this was found to be poorly behaved for the highly nonlinear flow in this relatively nondiffusive model, so a constant value was adopted. Consistent with the findings of Fovell and Ogura (1988), relatively large values of c^* were found to best replicate the behavior of simulations conducted in larger domains. In this specific application, the optimal value of c^* appears to be roughly 35 m s^{-1}. The influence of the lateral boundaries was further minimized by performing our computations in the widest practical domain (720 km). In this large domain, neither the lateral nor the upper boundaries were found to have a significant influence on the structure of the squall lines or their associated gravity waves.

3. The squall-line simulations

a. *Initial conditions*

For all simulations discussed herein, the thermodynamic structure was specified according to the analytic sounding of Weisman and Klemp (1982) shown in Fig. 1. This sounding was chosen since it has been frequently employed in cloud model simulations (e.g., Weisman and Klemp 1982; Rotunno et al. 1988; Weisman et al. 1988) and is known to support strong long-lived storms in environments of moderate shear in two-dimensional simulations. This sounding is conditionally unstable, possessing about 2400 J kg^{-1} of convective available potential energy with respect to a reference air parcel originating in the boundary layer. It also has significant negative buoyant energy below the level of free convection ($z_{LFC} \approx 1.25$ km). These characteristics are similar to those found for severe squall lines in springtime in Oklahoma by Bluestein and Jain (1985). As shown in Fig. 1, the reference parcel becomes negatively buoyant at about 10 km, well below the tropopause at 12 km. A constant mean relative humidity of 25% was specified throughout the stratosphere.

The horizontal wind soundings for each of the three simulations discussed in this paper are shown in Fig. 2. The three profiles are identical below 10 km; they have moderate wind shear in the lowest 2.5 km overlain by a layer of weaker shear. Previous investigators (e.g., Weisman et al. 1988; Fovell and Ogura 1989) have shown that storm structure is primarily determined by

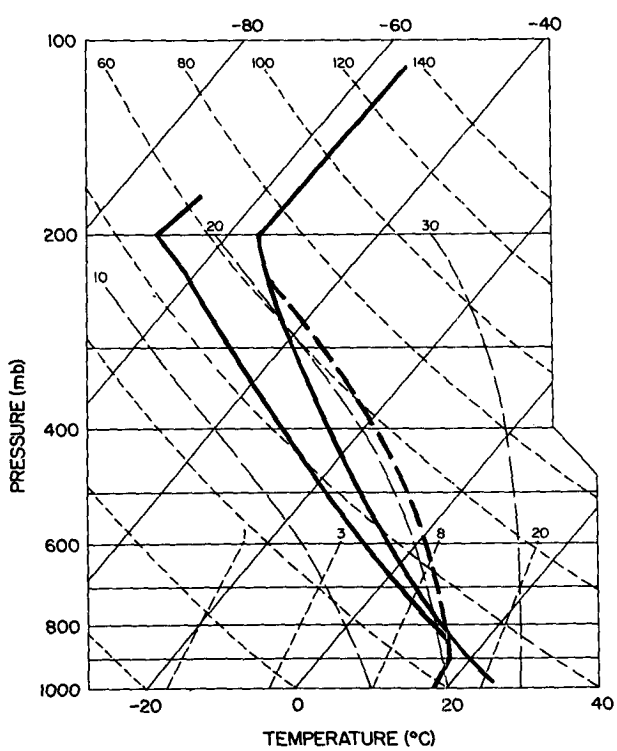

FIG. 1. Skew-T plot of the initial temperature and dewpoint soundings (heavy solid lines) for the cloud model. Dashed line shows temperature profile for moist-adiabatic ascent from the lifting condensation level at 900 mb. (After Weisman and Klemp 1982.)

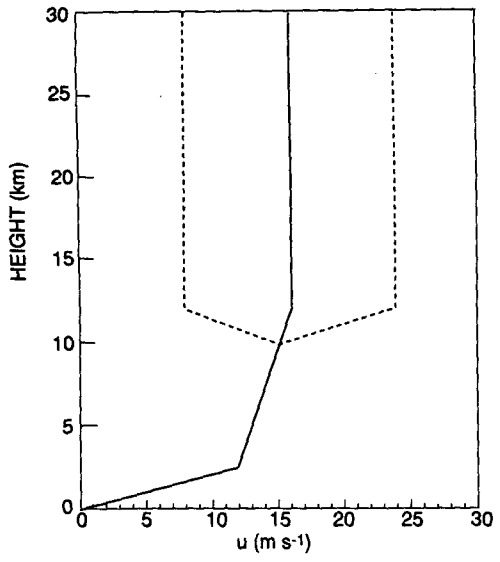

FIG. 2. Vertical profiles of mean zonal wind for the four cases discussed in the text.

the low-level wind shear and the convective available potential energy. Since these parameters were identical in all three cases, the deep convective clouds that developed in each simulation had very similar tropospheric structures. The time evolution of each storm was similar and, after organizing, they all propagated eastward at approximately 16 m s^{-1}.

In order to examine the influence of stratospheric storm-relative mean flow on the generation and propagation of gravity waves, the mean wind speed in the stratosphere was set to different values in the three cases. Both front-to-rear and rear-to-front relative flow were considered. These situations will be referred to as easterly and westerly flow, respectively (i.e., it is assumed that the positive x axis points eastward). There is almost no storm-relative flow in the control case $S(0)$. Case $S(-8)$ has 8 m s^{-1} easterly relative flow, and case $S(8)$ has 8 m s^{-1} westerly relative flow. In all cases the mean stratospheric winds are constant with height. The stratospheric and midtropospheric profiles are connected by a constant wind shear between the levels of 10 and 12 km. The mean-state Richardson number in this layer is large in all cases [Ri = 4.9 in the $S(8)$ case and Ri = 8.2 in the $S(-8)$ case].

The mean flow profile observed during the squall line of 22 May 1976, which was analyzed by Ogura and Liou (1980), lies between the $S(0)$ and $S(-8)$ cases. Their analysis showed tropospheric profiles similar to that specified in the model, weak storm-relative stratospheric flow with 5 m s^{-1} maximum westerlies near 14 km, and weak easterly shear above that level. Although easterly shear is a climatological feature of the extratropical lower stratosphere following the springtime final warming (Barnett and Corney 1985), in the simulations presented here the mean stratospheric wind shear is omitted in order to simplify the stratospheric gravity wave structure.

b. *The S(0) case*

The ground-relative stratospheric wind speed is equal to the propagation speed of the storm in the $S(0)$ case. Thus, the storm-relative mean stratospheric flow vanishes, and the stratospheric wave response may be studied for the simplest possible (zero motion) basic state. Owing to the favorable temperature and moisture structure of the Weisman and Klemp (1982) sounding, only a small ($\sim$2 K) moist thermal impulse is required to initiate the convection. As shown by Fovell and Ogura (1988), once convection begins, mesoscale storm organization occurs relatively quickly in the presence of moderate tropospheric shears. The evolution of this storm is similar to that of the storms simulated by Fovell and Ogura (1988); the reader is referred to their paper for details of the tropospheric structure and behavior.

The initial impulse generates a convective cell, which produces a substantial rainfall burst that reaches the ground within the first half hour. This can be seen in the x–t plot of rainfall intensity for the $S(0)$ simulation shown in Fig. 3. (The horizontal coordinate in Fig. 3 is a domain-relative coordinate, which moves eastward at 16 m s^{-1} relative to the ground, a speed chosen by trial and error to match the speed of translation of the storm. Thus, the position of the leading edge of the rainfall pattern remains nearly stationary in the translating coordinate frame.)

The initial cell is followed in quick succession by additional cells, each creating a rainfall burst. Convective cells in the early phase are narrow and intense. After about 3 h, however, the storm structure changes, and it begins producing somewhat weaker cells. These form episodically at the leading edge, grow upward, and propagate rearward at a speed of about 12.5 m s^{-1}, carrying precipitation toward the rear of the storm. They are separated by regions of convective downdrafts, and the net result is an oscillation in the surface rainfall rate. This behavior is typical of multicell storms.

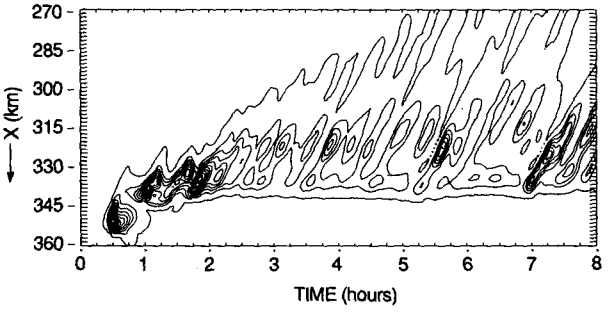

FIG. 3. Time–space plot of the rainfall rate in the control model storm. Distance is measured in a storm-relative coordinate moving at a speed of 16 m s^{-1} relative to the ground.

By 6 h, the width of the precipitating portion of the storm ceases to expand, but quasi-periodic cell production continues. The squall line at this time possesses many similarities to observed mature squall lines.

After the developing storm begins to precipitate, the evaporation of rainwater produces a pool of cold air at the surface beneath the region of active precipitation. When the cold pool is shallow, the updraft tilts toward the east (positive x direction) owing to advection by the ambient wind shear. The updraft becomes more vertical, and eventually acquires a westward (negative x direction) tilt as the cold pool intensifies and baroclinic vorticity generation at the leading edge of the cold pool begins to dominate the ambient horizontal vorticity in the low-level wind shear (Rotunno et al. 1988). In its mature phase, the storm updraft exhibits a pronounced westward tilt, and its dynamical and thermodynamical structures are similar to those in mature squall lines.

The overall structure of the simulated storm and the influence of the changes in the tilt of the updraft on gravity wave generation by the storm are illustrated in Figs. 4–6. These figures show x–z cross sections of various fields at 2, 4, and 6 hours into the simulation, respectively. Contours of the potential temperature are shown as light solid lines. (The location of the tropopause coincides approximately with the θ = 344 K contour, which is the contour that intersects the edges of the plot near the 12-km level.) The cloud outline, defined as the region in which the cloud-water mixing ratio exceeds 0.1 g kg^{-1}, is shown by a heavy solid line. The upper panel in each of these figures shows the storm-relative horizontal velocity contoured at 4 m s^{-1} intervals, with solid contours designating westerly winds and dashed contours easterly winds. The lower panels show vertical velocity, which is contoured at a 3 m s^{-1} interval in Fig. 4 and 1 m s^{-1} intervals in Figs. 5 and 6. Solid contours correspond to upward motion, and dashed contours to downward motion. (Only the central portion of the total computational domain is shown in these and subsequent figures.)

During the first 2 hours of the simulation the system is in its developing stage. By t = 2 h (Fig. 4) individual convective plumes within the main updraft of the developing storm have repeatedly overshot their levels of neutral buoyancy, penetrated into the stratosphere, and lifted the cloud top about 1 km above the tropopause in the region affected by the horizontal outflow of the overshooting plumes. The buoyancy force associated with the overshooting cells generates a series of gravity waves in the stratosphere. During this phase the storm produces waves with a variety of wavelengths and amplitudes on both its western and eastern sides. At t = 2 h, the waves are approximately symmetric about the updraft axis, as expected for waves produced by a vertically oriented, oscillating forcing in an atmosphere with no mean flow. (A mean storm-relative stratospheric flow would, of course, produce an asymmetry

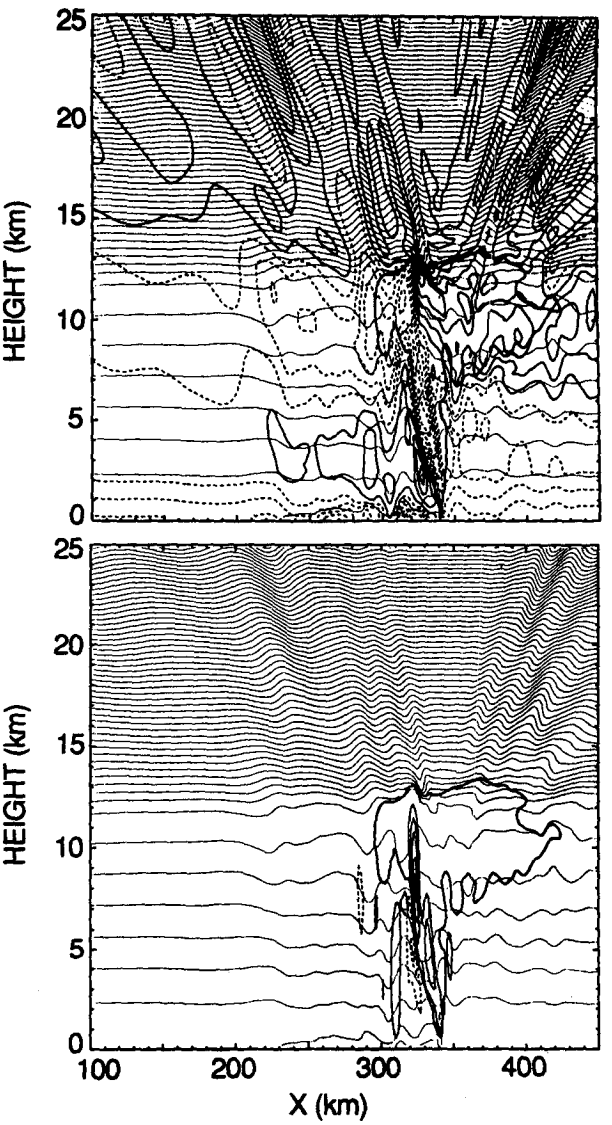

FIG. 4. Contours of zonal velocity (upper panel; contour interval 4 m s^{-1}) and vertical velocity (lower panel; contour interval 3 m s^{-1}) superposed on potential temperature contours (light lines, 4 K interval) and cloud outline (heavy solid line), defined as the region in which the cloud water-mixing ratio exceeds 0.1 g kg^{-1}; for the $S(0)$ case at t = 2 h.

between eastward- and westward-propagating gravity waves.) The waves on the eastern side are slightly stronger than their western counterparts. This may reflect the fact that the storm updraft was oscillating in orientation prior to this time, and periodically tilting toward the east as discussed previously. The x–z distribution of the waves in Fig. 4 suggests that they originate within the storm close to the level where the main updraft first becomes negatively buoyant (~10 km).

Storm behavior in the mature phase (t = 4 and 6 h, Figs. 5 and 6) is much different than during the development phase. A pronounced rear-inflow current,

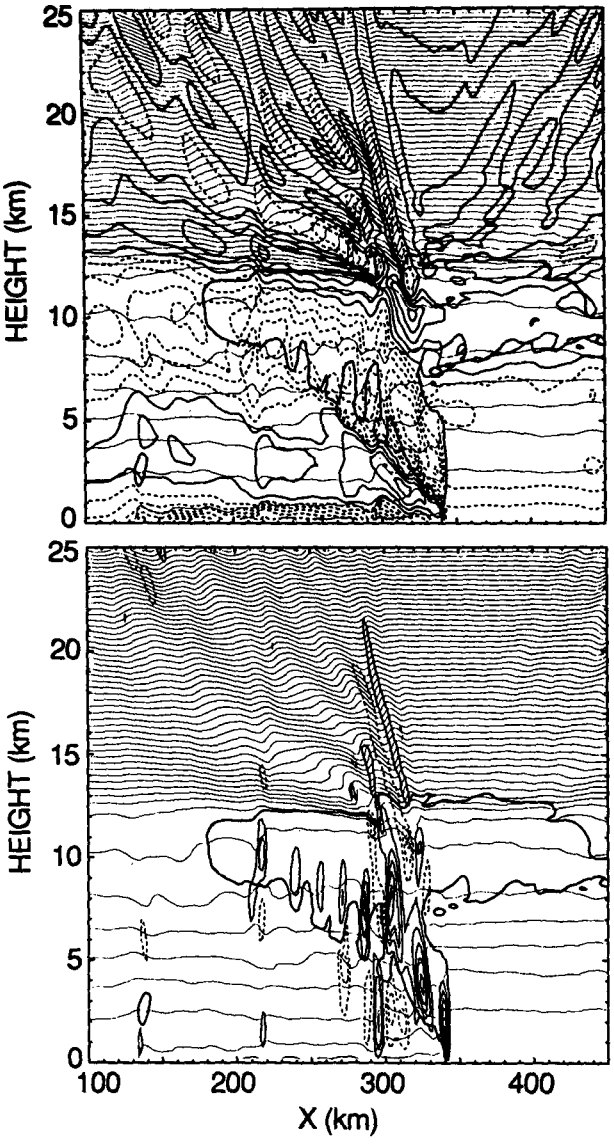

FIG. 5. As in Fig. 4 but for $t = 4$ h, except that in this case the contour interval for vertical velocity is 1 m s^{-1}.

with speeds in excess of 6 m s^{-1}, develops between the heights of 2 and 4 km and descends as it approaches the leading edge of the surface cold pool. Instead of a single vertically oriented updraft, which impulsively strikes the tropopause at one location, the mature storm is composed of a series of weaker cells embedded in a rising, westward-tilted airflow. These structures are found not only in the numerically simulated storm, but in Doppler radar observations of typical atmospheric squall lines (Smull and Houze 1987).

Because the updraft cells in the mature phase are less intense, the wave activity in the stratosphere is also weaker overall (recall that the contour interval for vertical velocity in Figs. 5 and 6 is one-third that in Fig. 4). In addition, the wave activity is now clearly biased to the western side. A "fan" of waves is present on this side, apparently sharing a common focus within the storm located about 2 km below the tropopause in the zone where the updraft air first becomes negatively buoyant. The lines of constant phase in the waves in Fig. 6 range from narrow, nearly vertically oriented rays directly above the region of strongest updrafts, where the cloud extends into the stratosphere, to nearly horizontal features extending far to the rear just above cloud top. The waves on the western side are similar at 4 h and 6 h (Figs. 5 and 6). The waves visible at 4 h well east of the storm have, however, propagated out of the domain by 6 h. Apparently, eastward-propagating waves are not generated during the mature phase.

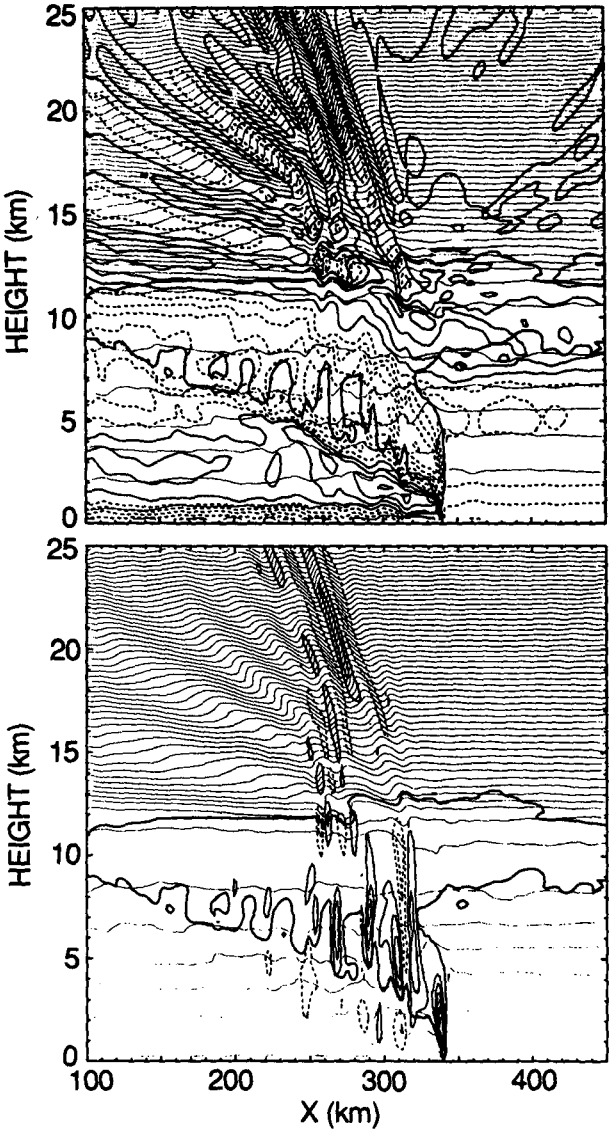

FIG. 6. As in Fig. 5 but for $t = 6$ h.

In the mature phase, cells develop at the leading edge of the storm, at low- to middle levels over the gust front, and rise upward as they travel rearward relative to the storm. (This is visible as a series of tropospheric updraft cells in the lower panels of Figs. 5 and 6.) Each updraft cell rapidly expands upward until it encounters the tropopause, producing a vertical displacement of the stable air layer in the vicinity of the tropopause. The maximum tropopause displacements occur toward the rear side of the region of elevated cloud top, and tend to move rearward with the motion of the cells. This behavior suggests that the tilt of the convective system and its individual cells, as well as rearward cell propagation, may account for the selective generation of rearward-propagating gravity waves. This hypothesis will be discussed in a later section.

Figures 5 and 6 clearly show that the maximum eastward and downward velocity perturbations associated with the stratospheric waves occur in phase with potential temperature surfaces sloping downward to the east of the maximum positive potential temperature perturbation, just as required for westward-propagating gravity waves. (It is intriguing to note that this correlation is clearly visible as an apparent shading in the region of positive zonal wind perturbations, owing to the packing together of isentropic surfaces in this region of enhanced stability.) As an aid to analysis, a time-lapse sequence of cross sections similar to those in Figs. 4–6 was generated from data at 2-minute intervals extending from $t = 5.5$ h to $t = 6.5$ h. The time sequence clearly showed that phase propagation of the stratospheric waves in the mature storm is westward and downward, while energy propagates westward and upward along ray paths parallel to phase lines.

The stratospheric waves in Figs. 4–6 obey the dispersion relationship for linear gravity waves in an isothermal, motionless basic state:

$$\omega^2 = N^2k^2/(k^2 + m^2 + \Gamma^2 + N^2/c_s^2), \quad (2)$$

where k and m are the horizontal and vertical wavenumbers, omega is the frequency, and

$$N^2 = \frac{2}{7} gH_s^{-1}, \quad c_s^2 = \frac{7}{5} gH_s, \quad \Gamma = \frac{3}{14} H_s^{-1}.$$

Here, $H_s = RT_0/g$ is the scale height, where T_0 is the isothermal temperature (Gill 1982, p. 172). Energy is propagated by the waves in the direction of the group velocity vectors, which are parallel to the lines of constant phase since the mean storm-relative flow is zero. If the small effects of compressibility are neglected, lines of constant phase tilt from the vertical at an angle θ such that

$$\theta = \cos^{-1}(\omega/N). \quad (3)$$

According to (3) the phase lines of the shortest-period waves are closest to the vertical, and the phase lines approach the horizontal as the period increases.

Figure 7 shows an analysis of the wave structure at selected locations in the stratospheric region behind the main tropospheric updraft 6 h after the beginning of the simulation. The local horizontal and vertical wavelengths were measured at the location of each of the six arrowheads in Fig. 7 and used to calculate the local period from the linear dispersion relation. The most vertically oriented waves have a period of 24 min (0.4 h), comparable to the average interval between the formation of new convective updrafts within the squall line. Note in particular that the rainfall bursts shown in Fig. 3 appear to have a 22-min average period in the 90-min interval prior to the time shown in Fig. 7. The horizontally oriented waves have periods of several hours, and appear to be generated by quasi-steady aspects of the squall-line circulation. The group velocity vector terminating at each of the six locations in Fig. 7 was also calculated from the wavelength data. The head of the group velocity vector was plotted at each data location, while the tail was plotted at an elevation of 12 km, 0.5 km below the cloud top (shown by the heavy dashed line) and near the region in which the waves appear to be generated. The 12-km level was also used to terminate the group velocity vector because it was the elevation of the mean-state tropopause, and the assumption of an isothermal atmosphere used in the derivation of (2) and the group velocity computations is appropriate only in the stratosphere. As predicted by theory, the group velocity vector is almost

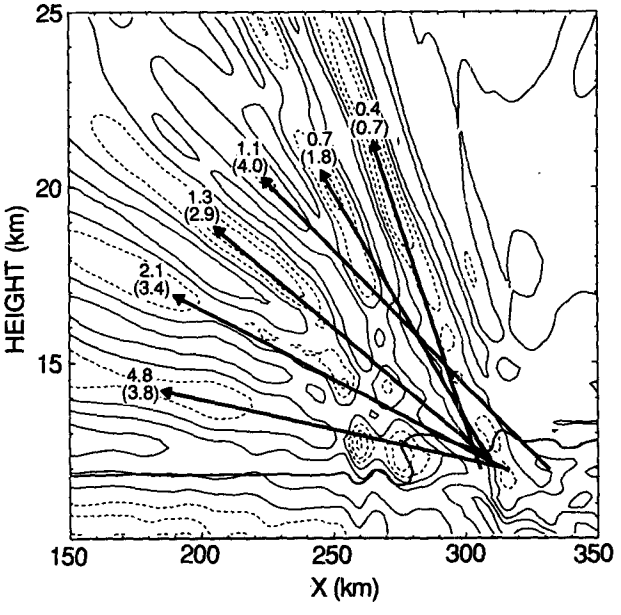

FIG. 7. Expanded view of storm-relative zonal wind in the stratosphere for case $S(0)$. Arrows show estimated group velocity paths for the wave packets located in the vicinity of each arrowhead at $t = 6$ h. The local wave period (in hours) is shown near the head of each arrow. Also indicated in parentheses is the time for a signal to propagate from the 12-km level to the location of each arrowhead.

parallel to the local line of constant phase passing through each data point in Fig. 7. The group velocity analysis shows that the energy source for the gravity waves is located in a compact region just below the cloud top. The time for a signal, traveling at the group velocity, to propagate from the 12-km level to each data point is also plotted (in parenthesis) in Fig. 7. These times range from 42 min for the shortest-period waves to 4 h for the longest-period waves.

The wave period deduced from (3) for the most vertically oriented waves can be confirmed from the time–height plot of the vertical velocity for a 1-h period centered at $t = 6$ h, shown in Fig. 8. The section is located at $x = 291$ km, a point about 50 km to the rear of the surface gust front. Below 12 km there are oscillating updrafts and downdrafts consistent with the rearward propagation of the aforementioned convective cells. Above 12 km the flow clearly consists of waves with downward phase propagation and upward energy propagation. The rate of downward phase propagation varies in time owing to the interference of waves of different frequencies. The dominant period range is about 20–25 min, consistent with the time scale for rainfall variation shown in Fig. 3.

c. *Influence of storm-relative stratospheric flow: The S(8) and S(−8) cases*

As discussed earlier, squall lines are most sensitive to the low-level wind shear and to the convective available potential energy. Since these variables remained unchanged in the cases with storm-relative stratospheric flow, the tropospheric structures of the squall lines in the $S(8)$ and $S(-8)$ simulations are quite similar to that in the $S(0)$ case. The evolution of the rainfall generated by the $S(8)$ and $S(-8)$ squall lines is plotted in Fig. 9, and may be compared with the $S(0)$ case shown in Fig. 3. As evidenced by these figures, all three storms evolved into their mature phases at about the same rate; they propagated at the same speed; and they had roughly similar multicellular structures. The time fluctuations in surface rainfall in the mature stage appear to have been more regular and of slightly higher frequency in the $S(-8)$ case; nevertheless, the general character of all three rainfall patterns is comparable.

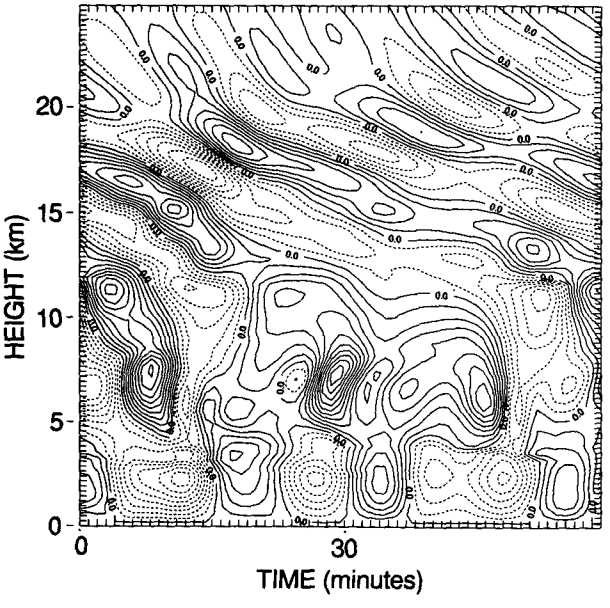

FIG. 8. Time–height section of vertical velocity at $x = 291$ km for the interval $t = 5.5$ h to $t = 6.5$ h in the $S(0)$ case.

On the other hand, the stratospheric gravity waves were strongly affected by the changes in the storm-relative stratospheric flow, particularly in the $S(8)$ case. Results from the $S(8)$ case are plotted in Fig. 10, which shows isentropes of potential temperature, the cloud outline, and contours of the storm-relative velocity. As in the $S(0)$ case (Fig. 6), only waves with westward-tilting phase lines are present in the stratosphere. However, unlike the $S(0)$ case, the tilt of the phase lines is relatively uniform. Animation shows that these waves are virtually steady.

The vertical wavenumber, m, for standing gravity waves in an isothermal atmosphere with constant mean wind U satisfies

$$m^2 = N^2/U^2 - k^2 - \Gamma^2 - N^2/c_s^2. \qquad (4)$$

Within the accuracy of the hydrostatic approximation (which is well satisfied by the long waves in Fig. 10), the vertical wavelength for stationary waves is $L_z = 2\pi U/N$, which for the $S(8)$ stratosphere gives $L_z = 2.4$ km. In Fig. 10 the local vertical wavelength of the stratospheric waves directly over the leading edge of the squall line is also 2.4 km, consistent with the evidence from animation that these waves are quasi-stationary. Waves east of the leading edge have slightly shorter vertical wavelengths, implying that their horizontal phase speeds are too slow to stand against the 8 m s^{-1} westerly stratospheric flow; indeed, animation shows these waves to be slowly propagating toward the east. Stratospheric waves west of the leading edge have wavelengths in excess of 2.4 km, phase speeds more negative than −8 m s^{-1}, and in the animation, appear to be slowly propagating upstream against the flow.

As demonstrated by the analysis of the $S(0)$ waves in Fig. 7, squall lines are capable of generating very low-frequency stratospheric waves. The low-frequency response is dramatically enhanced in the $S(8)$ case. Part of the enhanced steady-state response appears to be associated with the development of a very steady upper-level downdraft visible above the gust front (at $x = 340$ km) at an elevation of 9.5 km in Fig. 10b. The processes responsible for the generation of this persistent downdraft are the subject of continuing research. High-frequency waves associated with the 22-min period between convective updrafts are also present in the $S(8)$ case, although they are rather weak. These waves, which have almost vertically oriented

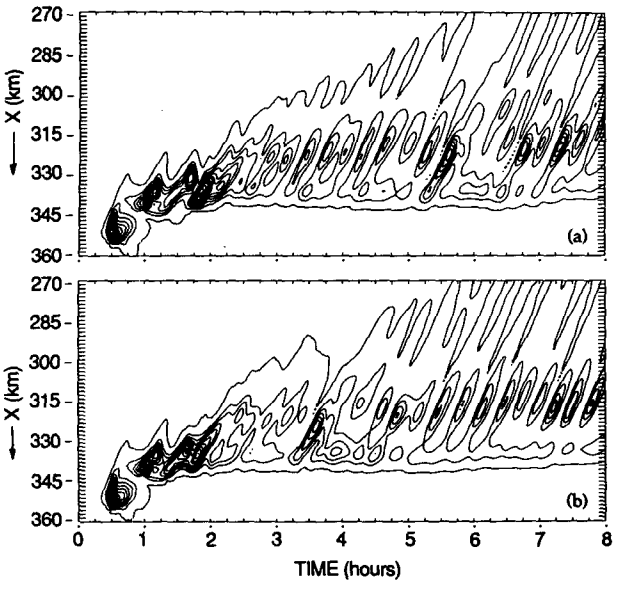

FIG. 9. As in Fig. 3 but for (a) the $S(+8)$ and (b) the $S(-8)$ case.

phase lines, are apparent in the animation as a modulation of the longer-wavelength response, but are difficult to see in Fig. 10.

The wave response in the $S(-8)$ case is shown in Fig. 11, which may be compared with Figs. 6 and 10. The overall wave amplitudes are somewhat weaker than those in the $S(0)$ and $S(8)$ cases. Westward-propagating high-frequency waves are generated near the top of the storm and appear similar to those in the $S(0)$ case. Once again, these high-frequency waves are closely associated with the periodic development of updrafts within the squall line. The connection between the oscillations of the storm updraft and the high-frequency gravity waves is apparent in the animation, and may also be appreciated by comparing two different calculations for their intrinsic frequency $\hat{\omega} = \omega - Uk$. In the vicinity of a point at $x = 200$ km, $z = 20$ km, the waves in the horizontal velocity field have a 20-km horizontal wavelength and a 3.2-km vertical wavelength. Using an isothermal stratospheric temperature of 217 K, the linear dispersion relation

$$\hat{\omega}^2 = N^2k^2/(k^2 + m^2 + \Gamma^2 + N^2/c_s^2) \qquad (5)$$

predicts a local intrinsic period of 31.6 min for these waves. Reference to Fig. 9b shows rainfall pulsations with an average period of 18 min during the 1½ h prior to the time shown in Fig. 11 (6 h). (The 18-min rainfall oscillation is even more regular during the final 2½ hours of the simulation.) Assuming the non-Doppler-shifted frequency ω of the forcing is equal to that of the rainfall pulsations, direct calculation of $2\pi/(\omega - Uk)$ yields an intrinsic period of 31.8 min, which agrees very well with the period calculated from the dispersion relation.

Low-frequency gravity waves are also apparent in the stratosphere in the $S(-8)$ case. Although they are weak, the waves east of the leading edge of the squall line are of particular interest. As in the $S(8)$ case, these waves have vertical wavelengths of almost 2.4 km, so their intrinsic horizontal phase speed ($\hat{\omega}/k$) is almost equal to that of the mean flow. The direction of propagation is, however, opposite to that in the $S(8)$ case. These waves propagate toward the east relative to the mean flow, but are rendered almost stationary by the 8 m s^{-1} storm-relative easterly flow. Thus, both cases with storm-relative stratospheric flow produce a standing wave response in the stratosphere. However, in the $S(8)$ case, the standing wave response is dominant, whereas the standing waves are very weak in the $S(-8)$ case.

As described in the Introduction, two possible generation mechanisms for convectively induced gravity waves have been proposed: the cloud-top obstacle effect

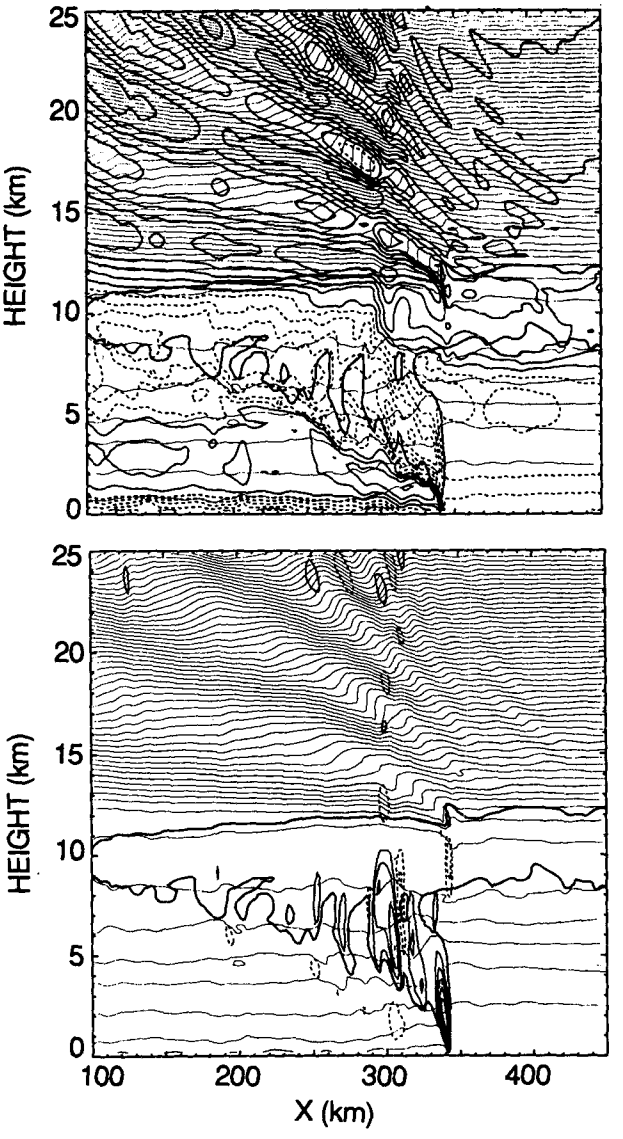

FIG. 10. As in Fig. 5 but for the $S(+8)$ case at $t = 6$ h.

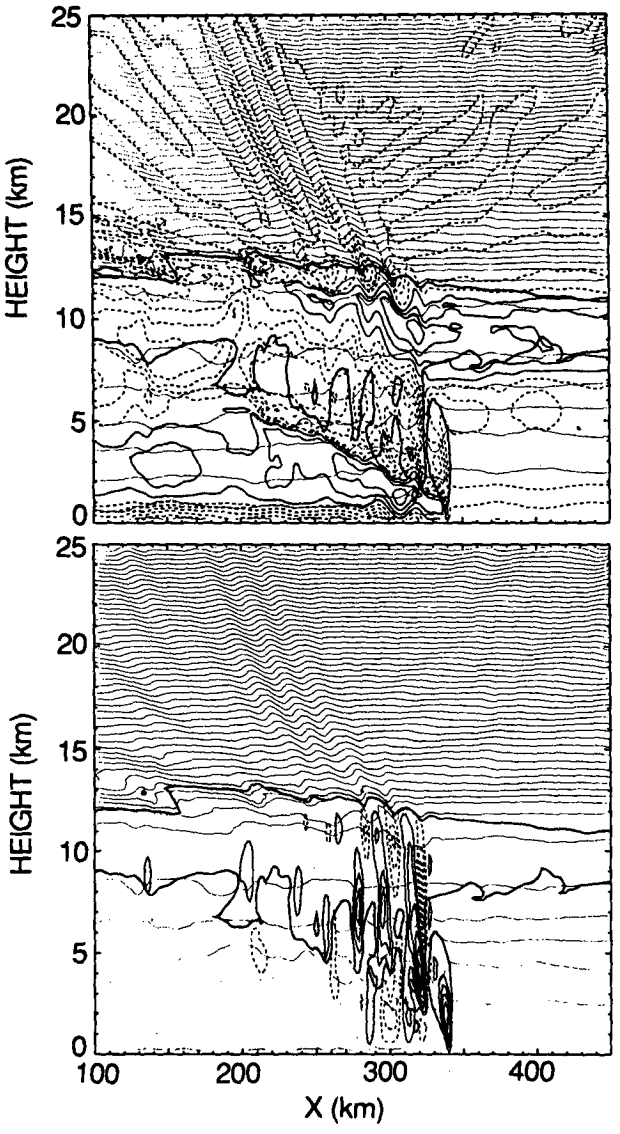

FIG. 11. As in Fig. 5 but for the $S(-8)$ case at $t = 6$ h.

(quasi-steady forcing) and mechanical excitation by parcel motions of individual updraft and downdraft cells. The three simulations just discussed suggest that both types of forcing may be significant, but that contrary to the boundary-layer convection cases studied by Clark et al. (1986), mechanical excitation is the more important of the two mechanisms, particularly for the higher-frequency waves. Quasi-steady forcing requires the presence of a moderately strong mean flow at the cloud top, and should not be active in the $S(0)$ case where storm-relative mean flow at cloud top is nearly absent. (It is, nevertheless, possible that an interaction between the storm-induced zonal winds in the lower stratosphere and the cloud updrafts might generate very low-frequency waves through quasi-steady forcing.) On the other hand, in all three cases mechanical excitation appears to generate the almost vertically oriented high-frequency waves. These waves, which have large vertical components of group velocity (see Fig. 7), could propagate to very high altitudes. Such convectively generated waves may contribute to the observed dominance of high-frequency (period less than 1 h) waves in the momentum budget of the mesosphere (e.g., Fritts and Vincent 1987).

To investigate possible sources for the high-frequency gravity waves produced in the cloud simulations [particularly in the $S(0)$ case] frequency power spectra of vertical velocity for several points within the simulated storms were analyzed (not shown). For example, the spectrum in the $S(0)$ case at a point in the stratosphere just above the main storm updraft shows significant power at frequencies corresponding to periods of 28, 21, and 16 min, among others. The largest power is at 21 min, which is in the neighborhood of the mean period of oscillation of the storm intensity (as manifested in the rainfall-rate diagram, Fig. 3). The dominant periods of oscillation at similar points in the other two model storms were approximately the same as found in the $S(0)$ case. The simulations with mean stratospheric flow tended to have more power in slightly shorter periods; the reason for this is not known. However, the dominant periods are confined to a fairly narrow range similar to the period range of the rainfall rate oscillations.

The presence of differing transition shear layers in the upper troposphere in the cases with mean storm-relative stratospheric flow implies that differences between the cases cannot be completely attributed to differing stratospheric mean winds; the transition layer coincides with the layer in which mechanical excitation occurs owing to the displacement of the isentropes by the updraft cells. Shear in this layer, which is substantial in the $S(-8)$ and $S(+8)$ runs, might have an important effect on the generation and transmission of gravity waves in this region.

4. Wave momentum fluxes

Theory and laboratory experiments in stratified fluids (see Lighthill 1978, Fig. 76) indicate that a mechanical oscillator of fixed frequency ω in a stratified fluid can generate gravity waves with positive and negative vertical phase tilts determined by the dispersion relation (2). Thus, if the convective cells generated quasi-periodically in the troposphere in the cloud model acted simply as vertical mechanical oscillators to force stratospheric gravity waves, propagation would occur not only along ray paths tilted westward and upward, but also along paths tilted eastward and upward at the same angle θ from the vertical. In such a case the net vertical momentum flux would be small, since the downward flux due to the westward-tilting waves would tend to be balanced by the upward flux due to the eastward-propagating waves. The fact that only westward-sloping waves are significantly excited in the mature phase of the $S(0)$ case indicates, however,

that significant net vertical momentum flux may occur in the cloud model.

In order to estimate the possible significance of the gravity wave momentum flux for stratospheric dynamics, the average fluxes for the region windowed in Figs. 6, 9, and 10 (i.e., x = 100 km to x = 450 km) were computed at t = 6 h. The results are shown for all three cases in Fig. 12. In the $S(-8)$ case the stratospheric waves are weaker, and there is some cancellation between the westward-propagating waves and the weak eastward-propagating waves, so there is little net momentum flux above the tropopause. In the $S(0)$ and $S(+8)$ cases, however, the strong westward-propagating waves produce a net momentum flux of order -0.2 N m^{-2}, which is locally comparable to values observed in topographically forced gravity waves (e.g., Lilly et al. 1982). A flux of -0.2 N m^{-2} at 16 km, which decays to zero at 26 km, implies a zonal wind forcing of 20 m s^{-1} d^{-1}, certainly a significant drag in the region of the storm. In midlatitude continental regions the average effects of such storm-generated stratospheric drag are probably much smaller than the drag produced by topographic waves. Over the tropical oceans, on the other hand, stratospheric drag induced by convective storms may be a significant contributor to the momentum budget.

5. A mechanical oscillator model

As we have seen above, only westward-sloping waves are significantly excited in the mature phase of the $S(0)$ case. This suggests that either the forcing does not excite the eastward-propagating branch or that this branch is in some manner rapidly damped above the tropopause. In fact, it appears that eastward-propagating waves are not forced by the mature squall line. There are two aspects of the squall-line circulation that seem to preferentially generate westward-propagating waves. The first (and, as will be shown later, the most important) factor is the storm-relative westward propagation of the individual convective cells associated with each upper-tropospheric updraft. The westward storm-relative propagation of these updrafts is evident in Figs. 3 and 9, and in time-lapse imagery from the numerical simulation (not shown). The second factor that might favor the production of westward-propagating waves is the westward tilt of the updraft/downdraft couplets associated with each convective cell. This tilt is illustrated in Fig. 13, which is a scatterplot of u' versus w' for the $S(0)$ case computed using time series data from three locations in the vicinity of upper-tropospheric updrafts and downdrafts. As is evident in Fig. 13, the correlation between u' and w' is large and negative, indicating a westward tilt to the upper-tropospheric convective cells.

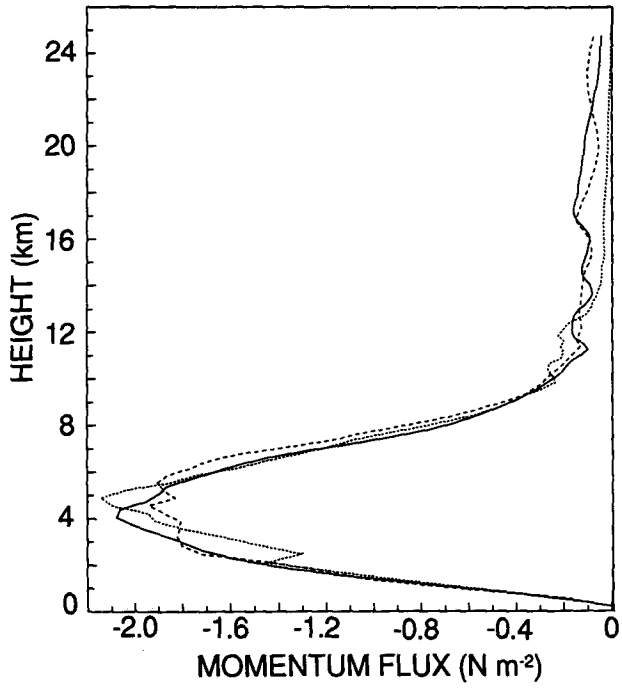

FIG. 12. Altitude profiles of vertical momentum flux (N m^{-2}) averaged from x = 100 to 450 km for the three cases. Solid line, $S(0)$; long dashes, $S(8)$; short dashes $S(-8)$.

In order to determine the effectiveness and relative importance of cell propagation and cell tilt in the preferential excitation of westward-propagating gravity waves, a series of simulations were conducted in which gravity waves were generated by an idealized oscillatory source. For computational convenience, these "mechanical oscillator" model calculations were made with the version of the Klemp–Wilhelmson model that Fovell (1991) used for idealized heat source calculations. This model is similar to that used for the squall-line simulations in most important respects. The domain was 360 km wide and 21.7 km deep with constant grid resolution of 2.0 km in the horizontal and 700 m in the vertical. The static stability profile was the same as that used in the convective-storm simulations. The forcing in this model consisted of an oscillatory momentum source whose spatial structure was specified as a streamfunction in the x–z plane. The forced momentum equations for the oscillator model take the following form:

$$\frac{Du}{Dt} + \frac{1}{\rho_0}\frac{\partial p}{\partial x} = -\frac{1}{\rho_0}\frac{\partial \Psi}{\partial z} \tag{6a}$$

$$\frac{Dw}{Dt} + \frac{1}{\rho_0}\frac{\partial p}{\partial z} + g\frac{\rho'}{\rho_0} = \frac{1}{\rho_0}\frac{\partial \Psi}{\partial x} \tag{6b}$$

where the terms on the right are the momentum source terms that are intended to approximate forcing by propagating convection cells. The forcing function is specified to have the form

$$\Psi(x, z, t) = \frac{G(x, z, t)h_0(x, z)}{[1 + (x - x_0)^2/a^2 + (z - z_0)^2/b^2]} \tag{7}$$

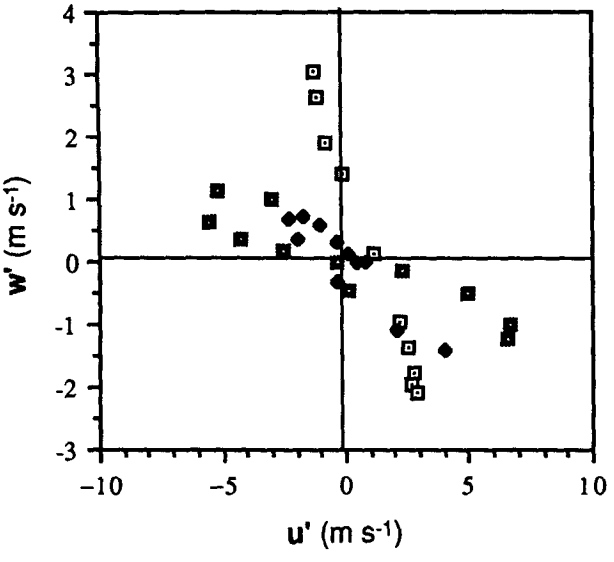

FIG. 13. Scatter plot of u' versus w' sampled at three locations in the upper-tropospheric updraft/downdraft region for the $S(0)$ simulation.

where

$$G(x, z, t) = \begin{cases} \sin[k(x - x_0)] \cos[m(z - z_0)] \sin\omega t & \text{Case 1} \\ \sin[k(x - x_0) + m(z - z_0)] \sin\omega t & \text{Case 2} \\ \cos[k(x - x_0) + m(z - z_0) + \omega t] & \text{Case 3} \\ \sin[k(x - x_0) + \omega t] \sin[m(z - z_0)] & \text{Case 4} \end{cases}$$

and

$$h_0(x, z) = \begin{cases} (40 \text{ kg m}^{-1} \text{ s}^{-2}), & \text{for } |k(x - x_0)| < \pi, \\ & \text{and } |m(z - z_0)| < \pi \\ 0, & \text{for } |k(x - x_0)| \geq \pi, \\ & \text{and } |m(z - z_0)| \geq \pi. \end{cases}$$

Here $x_0 = 360$ km (the midpoint of the domain), $z_0 = 8$ km, $a = 10$ km, $b = 1$ km, $k = 2\pi/(20 \text{ km})$, $m = 2\pi/(6 \text{ km})$, and $\omega = 2\pi/(20 \text{ min})$. This form of source function represents an oscillator, varying periodically in space and time, whose amplitude envelope is restricted to a small region in space centered about (x_0, z_0).

In case 1 the source has the form of a vertically oriented standing-wave oscillation, which can be interpreted as a combination of eastward- and westward-propagating waves with the same amplitude. In case 2 the forcing is a standing wave concentrated along a path whose angle to the vertical is given by $\tan\theta = k/m$. This case tests the effects of an oscillator that is fixed in space, but tilts westward with height. In case 3 the forcing pattern tilts westward with height as in case 2, and propagates westward at a phase speed appropriate to gravity waves with wavenumber ratio k/m. Case 4 has westward propagation of the source as in case 3, but the oscillator is vertically oriented. These cases are designed to investigate the relative importance of oscillator tilt versus rearward propagation in accounting for the asymmetric gravity wave distributions characteristic of the cloud model cases previously discussed.

The perturbation temperature response at $t = 4$ h is shown in Fig. 14a for case 1. The response in this case is symmetric about the domain center, as would be expected for symmetric forcing in the absence of a mean wind. Waves propagate upward from the source region along ray paths parallel to lines of constant phase whose angle of tilt from the vertical ($\sim 74°$) is in approximate agreement with (3).

As was shown in Fig. 13, during the mature stage of a simulated storm the updrafts are tilted toward the rear of the storm. Thus, they might be expected to preferentially excite gravity waves with phase lines tilting toward the rear with height. In order to test this hypothesis we set the ratio of m and k in the source function for the mechanical oscillator to a value corresponding to the predicted slope of a linear gravity wave of period 20 min. The resulting wave pattern is shown in Fig. 14b. Clearly, a tilted mechanical oscillator, by primarily exciting parcel oscillations that slope in the same sense as the source, can produce a highly asymmetric gravity wave response. This strongly supports our view that the wave generation in the cloud model control case is due to forcing by a mechanical oscillator effect.

Although the left-tilting waves are considerably amplified in Fig. 14b when compared to Fig. 14a, there is still some propagation into the region to the right of the source. Therefore, rearward tilt of the mechanical oscillator is not sufficient to completely eliminate the right-tilting waves. The source still has the structure of a standing-wave oscillator, and hence produces a response that propagates both eastward and westward. The tilt of the source simply increases the efficiency of excitation for the westward-propagating mode.

The updraft cells in the storm simulations not only have westward tilt, but they also propagate toward the rear of the storm, with new cells developing at about a 20-min interval. This behavior was incorporated in the mechanical oscillator model in case 3, in which the source not only tilts as in case 2, but also propagates to the west. [Note that the amplitude is defined by an envelope restricted to the vicinity of (x_0, z_0).] The wave pattern excited by this source is shown in Fig. 14c. In this case, the rightward-tilting waves are completely eliminated and the wave pattern is very similar to that of the high-frequency waves in the control model case shown in Fig. 5. Case 4 is similar to case 3 except that the source is vertically oriented and westward propagating. Again only the westward-tilting waves are excited by the source. Apparently, rearward propagation of the source is essential in accounting for the highly

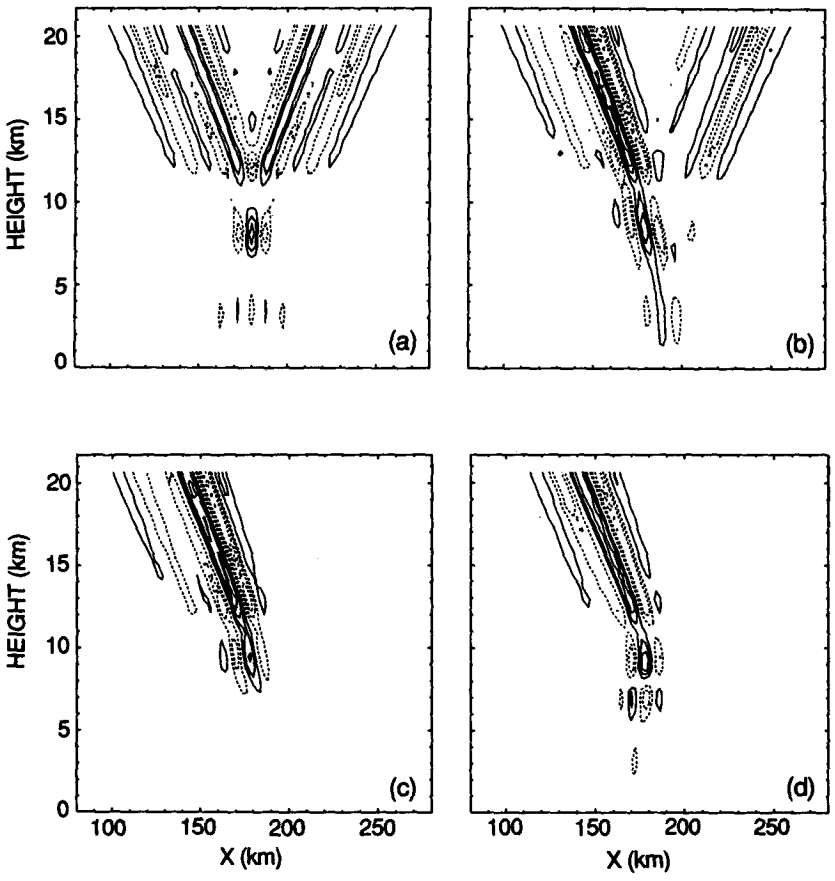

FIG. 14. Perturbation potential temperature distribution in the mechanical oscillator model with $\bar{u} = 0$. (a) Vertically oriented standing wave momentum source; (b) tilted standing wave momentum source; (c) tilted propagating momentum source; (d) propagating momentum source, but no tilt.

asymmetric wave pattern in the absence of storm-relative mean flow in the stratosphere.

These results are similar to the wave patterns produced in the laboratory experiments summarized in Lighthill (1978). In most of these experiments a compact cylindrical obstacle was forced to oscillate at fixed frequency in a salt-stratified solution with a constant buoyancy frequency. In some cases (e.g., Stevenson and Thomas 1969) the oscillating cylinder also had a mean motion relative to the stratified fluid, which is dynamically equivalent to a stationary oscillating cylinder in a mean flow. For a cylinder oscillating horizontally or vertically at fixed frequency ω in a motionless basic state the response is in the form of a "St. Andrews cross," with ray paths whose angle θ to the vertical is given by (1).[1]

In order to examine the effect of mean flow we added a uniform -8 m s^{-1} mean wind. The resulting perturbation temperature field is shown in Fig. 15 for forcing equivalent to that of case 1 (see Fig. 14a). The response clearly shows the effect of Doppler shifting. The waves have phase lines whose tilts from the vertical are approximately given by the Doppler-shifted version of (3):

$$\theta = \cos^{-1}\left(\frac{\omega \pm Uk}{N}\right) \tag{8}$$

where the minus sign is for waves upstream (to the east) of the source and the plus sign for waves downstream (to the west) of the source. (Note that $U = -8$ m s^{-1} for this situation.) The increase in the tilt of the phase lines from the vertical west of the source in Fig. 15 in comparison with Fig. 14a is similar to the change in the tilt of the most vertically oriented phase lines between Figs. 6 and 10, which suggests that the difference in the structure of the waves from the $S(0)$ case to the $S(-8)$ case is a result of Doppler shifting by the stratospheric mean flow.

One aspect of the cloud model that the single-frequency mechanical oscillator model does not mimic

[1] The bottom half of the St. Andrews cross was also generated in the simulations shown in Fig. 14, but it is not apparent because the potential temperature perturbations in the weakly stratified troposphere are small.

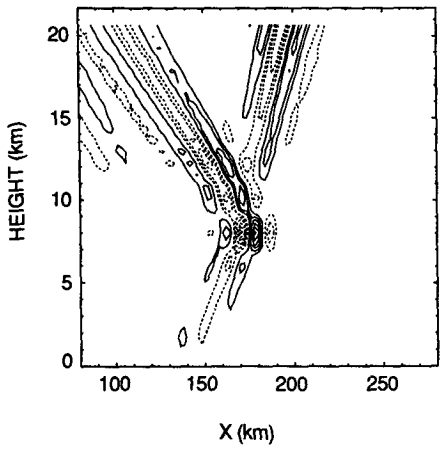

FIG. 15. As in Fig. 14a but for a vertically oriented standing-wave momentum source with $\bar{u} = -8$ m s^{-1}.

is the fanlike distribution of waves of varying slope that propagate rearward, particularly in the $S(0)$ case (e.g., Fig. 7). As previously discussed, the frequency spectra of the updrafts in the storm simulations contain several peaks. It is likely that the fanlike appearance of waves in the cloud simulations is due to simultaneous forcing at several frequencies. To test this hypothesis in the oscillator model a tilted source was utilized, with three separate periods of 15, 20, and 50 min. Provided that source tilts appropriate to each specific frequency are used, the response in this case (not shown) has a fanlike character similar to that in the cloud model and is consistent with the multiple forcing frequency hypothesis.

6. Conclusions

The preceding two-dimensional numerical simulations suggest that large-amplitude stratospheric gravity waves can be generated by long-lived squall lines. These waves are present in cases with and without stratospheric storm-relative flow, suggesting that the "obstacle" effect does not play an important role in their generation. It appears that the primary wave-generation mechanism is provided by convective updrafts, which periodically form at low levels near the forward edge of the squall line, move rearward, and ascend until they encounter the tropopause. The average period of the updraft forcing matches the 18–24-min Doppler-shifted period of the highest-frequency gravity waves. The action of the updraft cells is, therefore, analogous to that of a mechanical oscillator.

Longer-period stratospheric waves are also generated in these simulations, particularly in the cases with 0 and 8 m s^{-1} storm-relative mean flow in the stratosphere [the $S(0)$ and $S(8)$ cases]. The persistent upper-tropospheric downdraft that appears above the surface gust front in the $S(8)$ case may be associated with the generation of waves through an obstacle effect. Nevertheless, the presence of long-period waves in the case with no stratospheric storm-relative flow, $S(0)$, suggests that obstacle effects are not essential for the generation of such quasi-steady waves.

In the initial stage of squall-line development, the convective updrafts generated both eastward- and westward-propagating stratospheric gravity waves. Significant vertical fluxes of horizontal momentum are associated with both wave trains. The net momentum flux averaged over the entire domain is, nevertheless, small because the transports in the eastward- and westward-propagating waves almost cancel. On the other hand, in the mature stage of the squall line, the only stratospheric waves forced by the storm were those propagating westward toward the rear of the storm. In the absence of compensating transport by eastward-propagating waves, the domain-averaged momentum flux is significant. In the $S(0)$ and $S(8)$ cases, the stratospheric momentum flux is approximately 5% of the maximum momentum flux produced by convective overturning in the midtroposphere. The momentum transports in the stratosphere are, therefore, unlikely to exert a major influence on the squall-line circulation. Those transports could, however, constitute significant parts of the stratospheric and mesospheric momentum budgets.

In order to determine why only the westward-propagating high-frequency gravity wave branch was generated in the mature phase of the storm, integrations were carried out with a simple mechanical oscillator model. These simulations showed that, although the east–west tilt of the oscillator exerted a significant influence on the relative strength of the eastward and westward waves, the most important factor was not tilt, but the presence or absence of horizontal propagation in the oscillatory forcing. A westward-propagating oscillator generated only westward-propagating waves, regardless of its tilt. On the other hand, a standing-wave oscillator produced some eastward-propagating response, even when the oscillator was tilted so that the forcing projected primarily along a path parallel to phase lines of the westward-propagating mode (i.e., parallel to the group velocity vector of the westward-propagating waves). Thus, we conclude that the storm-relative motion of updraft cells, which is characteristic of squall lines, caused the simulated storms primarily to produce gravity waves with phase propagation toward the rear of the storm.

In the simulations reported here, the mean flow in the stratosphere was specified to be constant with height to facilitate comparison with linear gravity wave theory. In reality there is generally vertical shear in the lower stratosphere, and under some conditions gravity waves generated by squall lines might encounter critical levels. Three-dimensional effects may also play an important role in determining the magnitude of real-world convectively generated momentum fluxes. These possibilities will be the subject of future simulations.

Acknowledgments. This material is based upon work supported by the Physical Meteorology Program of the National Science Foundation under Grant ATM-8813971, and in part by NASA Grant NAGW-662. Computer time was provided by the National Center for Atmospheric Research.

REFERENCES

Andrews, D. G., J. R. Holton, and C. B. Leovy, 1987: *Middle Atmospheric Dynamics.* Academic Press, 489 pp.

Barnett, J. J., and M. Corney, 1985: *Middle Atmosphere Reference Model Derived from Satellite Data.* Handbook MAP, SCOSTEP Secretariat, 47–85.

Bluestein, H. B., and M. H. Jain, 1985: Formation of mesoscale lines of precipitation: Severe squall lines in Oklahoma during spring. *J. Atmos. Sci.*, **42,** 1711–1732.

Bretherton, C., 1988: Group velocity and the linear response of stratified fluids to internal heat or mass sources. *J. Atmos. Sci.*, **45,** 81–93.

Clark, T. L., T. Hauf, and J. P. Kuettner, 1986: Convectively forced internal gravity waves: Results from two-dimensional numerical experiments. *Quart. J. Roy. Meteor. Soc.*, **112,** 899–925.

Durran, D. R., 1986: Another look at downslope windstorms. Part I: On the development of analogs to supercritical flow in an infinitely deep, continuously stratified fluid. *J. Atmos. Sci.*, **43,** 2527–2543.

——, and J. B. Klemp, 1983: A compressible model for the simulation of moist mountain waves. *Mon. Wea. Rev.*, **111,** 2341–2361.

Fovell, R. G., 1991: Influence of the Coriolis force on two-dimensional model storms. *Mon. Wea. Rev.*, **119,** 606–630.

——, and Y. Ogura, 1988: Numerical simulation of a midlatitude squall line in two dimensions. *J. Atmos. Sci.*, **45,** 3846–3879.

——, and ——, 1989: Effect of vertical wind shear on numerically simulated multicell storm structure. *J. Atmos. Sci.*, **46,** 3144–3176.

Fritts, D. C., 1984: Research status and recommendations from the Alaska workshop on gravity waves and turbulence in the middle atmosphere. *Bull. Amer. Meteor. Soc.*, **65,** 149–159.

——, and R. A. Vincent, 1987: Mesospheric momentum flux studies at Adelaide, Australia: Observations and a gravity wave–tidal interaction model. *J. Atmos. Sci.*, **44,** 605–619.

Gage, K. S., and B. B. Balsley, 1984: MST radar studies of wind and turbulence in the middle atmosphere. *J. Atmos. Terr. Phys.*, **46,** 739–753.

Gill, A. E., 1982: *Atmosphere–Ocean Dynamics.* Academic Press, 662 pp.

Haynes, P. H., C. J. Marks, M. E. McIntyre, T. G. Shepherd, and K. P. Shine, 1991: On the "downward control" of extratropical diabatic circulations by eddy-induced mean zonal forces. *J. Atmos. Sci.*, **48,** 651–678.

Holton, J. R., 1983: The influence of gravity wave breaking on the general circulation of the middle atmosphere. *J. Atmos. Sci.*, 2497–2507.

Klemp, J. B., and R. B. Wilhelmson, 1978: The simulation of three-dimensional convective storm dynamics. *J. Atmos. Sci.*, **35,** 1070–1096.

——, and D. R. Durran, 1983: An upper boundary condition permitting internal gravity wave radiation in numerical mesoscale models. *Mon. Wea. Rev.*, **111,** 430–444.

Kuettner, J. P., P. A. Hildebrand, and T. L. Clark, 1987: Convection waves: Observations of gravity wave systems over convectively active boundary layers. *Quart. J. Roy. Meteor. Soc.*, **113,** 445–467.

Lighthill, J., 1978: *Waves in Fluids.* Cambridge University Press, 504 pp.

Lilly, D. K., J. M. Nicholls, R. M. Chervin, P. J. Kennedy, and J. B. Klemp, 1982: Aircraft measurements of wave momentum flux over the Colorado Rocky Mountains. *Quart. J. Roy. Meteor. Soc.*, **108,** 625–642.

Lindzen, R. S., 1981: Turbulence and stress owing to gravity wave and tidal breakdown. *J. Geophys. Res.*, **86,** 9707–9714.

Lu, D., T. E. VanZandt, and W. L. Clark, 1984: VHF Doppler radar observations of buoyancy waves associated with thunderstorms. *J. Atmos. Sci.*, **41,** 272–282.

Mahlman, J. D., and L. J. Umscheid, 1987: Comprehensive modeling of the middle atmosphere: The influence of horizontal resolution. *Transport Processes in the Middle Atmosphere,* G. Visconti, Eds., D. Reidel, 251–256.

Mason, P. J., and R. I. Sykes, 1982: A two-dimensional numerical study of horizontal role vortices in an inversion capped boundary layer. *Quart. J. Roy. Meteor. Soc.*, **108,** 801–823.

McFarlane, N. A., 1987: The effect of orographically excited gravity wave drag on the general circulation of the lower stratosphere and troposphere. *J. Atmos. Sci.*, **44,** 1775–1800.

Miller, M. J., T. N. Palmer, and R. Swinbank, 1989: Parameterization and influence of subgridscale orography in general circulation and numerical weather prediction models. *Meteor. Atmos. Phys.*, **40,** 84–109.

Miller, P. P., and D. R. Durran, 1991: On the sensitivity of downslope windstorms to the asymmetry of the mountain profile. *J. Atmos. Sci.*, **48,** 1457–1473.

Ogura, Y., and M. T. Liou, 1980: The structure of a midlatitude squall line: A case study. *J. Atmos. Sci.*, **37,** 553–567.

Orlanski, I., 1976: A simple boundary condition for unbounded hyperbolic flows. *J. Comput. Phys.*, **21,** 251–269.

Palmer, T. N., G. J. Shutts, and R. Swinbank, 1986: Alleviation of a systematic westerly bias in general circulation and numerical weather prediction models through an orographic gravity wave drag parameterization. *Quart. J. Roy. Meteor. Soc.*, **112,** 1001–1039.

Pfister, L., W. Starr, R. Craig, and M. Loewenstein, 1986: Small-scale motions observed by aircraft in the tropical lower stratosphere: Evidence for mixing and its relationship to large-scale flows. *J. Atmos. Sci.*, **43,** 3210–3225.

Rind, D., R. Suozzo, N. K. Balachandran, A. Lacis, and G. Russell, 1988: The GISS global climate–middle atmosphere model. Part I: Model structure and climatology. *J. Atmos. Sci.*, **45,** 329–370.

Rossby, C. G., 1938: On the mutual adjustment of pressure and velocity distributions in certain simple current systems. II. *J. Mar. Res.*, **2,** 239–263.

Rotunno, R., J. B. Klemp, and M. L. Weisman, 1988: A theory for strong, long-lived squall lines. *J. Atmos. Sci.*, **45,** 463–485.

Smith, R. B., and Y.-L. Lin, 1982: The addition of heat to a stratified airstream with application to the dynamics of orographic rain. *Quart. J. Roy. Meteor. Soc.*, **108,** 353–378.

Smull, B. F., and R. A. Houze, 1987: Rear inflow in squall lines with trailing stratiform precipitation. *Mon. Wea. Rev.*, **115,** 2869–2889.

Stevenson, T. N., and N. H. Thomas, 1969: Two-dimensional internal waves generated by a travelling oscillating cylinder. *J. Fluid Mech.*, **36,** 505–511.

Weisman, M. L., and J. B. Klemp, 1982: The dependence of numerically simulated convective storms on vertical wind shear and buoyancy. *Mon. Wea. Rev.*, **110,** 504–520.

——, ——, and R. Rotunno, 1988: The structure and evolution of numerically simulated squall lines. *J. Atmos. Sci.*, **45,** 1990–2013.

Zhu, X., and J. R. Holton, 1987: Mean fields induced by local gravity-wave forcing in the middle atmosphere. *J. Atmos. Sci.*, **44,** 620–630.